Journal of Materials Chemistry A

ROYAL SOCIETY OF CHEMISTRY

PAPER

View Article Online
View Journal | View Issue

Cite this: J. Mater. Chem. A, 2025, 13, 9923

High yield ammonia production *via* glucose oxidation assisted electrochemical nitrate reduction†

Akansha Chaturvedi,‡ Sukhjot Kaur,‡ Kalpana Garg and Tharamani C. Nagaiah *

The electrocatalytic nitrate (NO_3^-) reduction reaction (NO_3RR) provides a potential route for the synthesis of value-added ammonia (NH_3) and removal of nitrate pollutants. However, this reaction is limited by nitrate adsorption and slow kinetics involving multiple proton and electron transfer steps. The sluggish OER can hinder NO_3RR performance, but replacing it with a more facile oxidation process enhances performance. Herein, we have demonstrated the glucose oxidation assisted NO_3RR, utilizing CuNi(1 : 2)S as a bifunctional catalyst demonstrating a high NH_3 faradaic efficiency (F.E.) of 93.44% with a yield rate of 4.7 mg h^{-1} cm^{-2} or 280.47 mmol g_{cat}^{-1} h^{-1} at −0.4 V *vs.* RHE along with achieving high current densities of ~118 mA cm^{-2} and its high activity compared to monometallic variants was explained using the ultraviolet photoelectron spectroscopy (UPS) technique. Furthermore, a mechanistic study using *in situ* electrochemical Raman spectroscopy, illustrates the hydrogenation of NO_3^- to NH_3 *via* a NO_2^- intermediate. Moreover, replacing the OER with the glucose oxidation reaction (GOR) in a full cell system could decrease the total energy input by 200 mV and increase the NH_3 yield from 120.95 μg h^{-1} cm^{-2} to 259.46 μg h^{-1} cm^{-2}. Furthermore, high value-added products were obtained at both the anode and cathode at a low cell voltage. More interestingly, we demonstrate the practical extraction of high-purity NH_4Cl(s) and NH_3 aqueous products from electro-reduced NO_3^- after electrolysis at 100 mA cm^{-2} for 50 h, with a collection efficacy of 89.84% for the condensed NH_3(aq) solution.

Received 16th October 2024
Accepted 23rd February 2025

DOI: 10.1039/d4ta07397e

rsc.li/materials-a

Introduction

Hydrogen energy is being touted as an appealing substitute for fossil fuels in light of the rising need to reduce carbon emissions.[1] However, challenges with H_2 storage and transportation hinder its scalability.[2] Amidst these challenges, ammonia (NH_3) emerges as a key player in clean hydrogen deployment due to its high volumetric energy density (12.92–14.4 MJ L^{-1}), high hydrogen content (17.65%), and easy liquefaction.[3–8] NH_3 is also crucial for fertilizer production, addressing the UN's Sustainable Development Goal of Zero Hunger.[9,10] With an annual demand exceeding 200 million metric tonnes, NH_3 is the second most synthesized feedstock globally.[11] Currently, NH_3 production relies on the energy-intensive Haber–Bosch process, consuming about 1% of the world's fossil-fuel energy and emitting over 400 million metric tons of CO_2 annually.[4,12–16] Recently, electrochemical nitrogen reduction (NRR) to ammonia has emerged as a sustainable alternative.[4,17,18] However, challenges such as the activation of the inert dinitrogen triple bond, low water solubility of N_2, and the competing hydrogen evolution reaction (HER) result in low faradaic efficiency (F.E.) and NH_3 yield, falling short of the U.S. Department of Energy's targets (DoE, F.E.: 50% and an NH_3 yield rate of over 1700 μg h^{-1} cm^{-2}).[19–24] The electrochemical nitrate reduction reaction (NO_3RR) to ammonia offers a glimmer of hope, due to the lower bond dissociation energy of the N=O bond (204 kJ mol^{-1}) compared to N≡N (941 kJ mol^{-1}) and higher water solubility (316 g L^{-1} at 20 °C).[25–27] Moreover the NO_3RR has the potential to generate NH_3 from polluted industrial and agricultural wastewater, aiding in environmental remediation.[25,26,28,29]

Furthermore, the overall nitrate electrolysis pairs up with the NO_3RR ($NO_3^- + 7H_2O + 8e^- \rightarrow NH_4OH + 9OH^-$) at the cathode and the OER ($4OH^- \rightarrow O_2 + 2H_2O + 4e^-$) at the anode. However, the slow kinetics associated with the O–O bond formation and the requirement of four proton-coupled electron transfer demand high energy input making NO_3^- electrolysis in the NO_3RR–OER pair an energy intensive process.[30,31] Moreover, the OER doesn't provide us with an industrially relevant product. Hence, replacing the OER with alternative anodic reactions which are thermodynamically favourable has become an emerging solution to address the "energy-saving" issue in the NO_3RR–OER electrolysis. Therefore, owing to lower overpotential required compared to the OER, the GOR ($C_6H_{12}O_6 + 2OH^- \rightarrow C_6H_{12}O_7 + 2H_2O + 2e^-$ and

Department of Chemistry, Indian Institute of Technology Ropar, Rupnagar-140001, Punjab, India. E-mail: tharamani@iitrpr.ac.in

† Electronic supplementary information (ESI) available. See DOI: https://doi.org/10.1039/d4ta07397e

‡ These authors contributed equally.

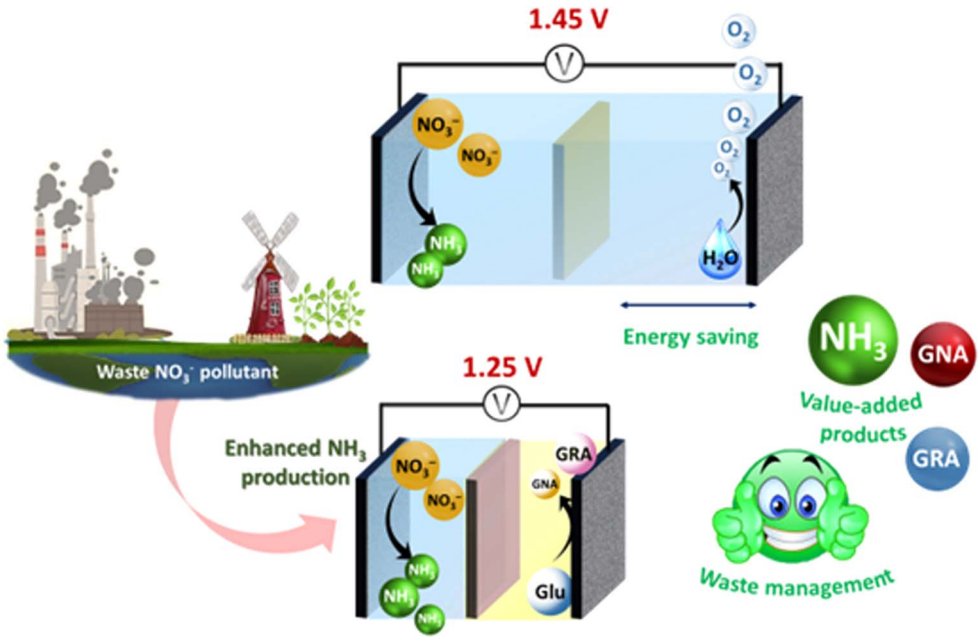

Fig. 1 Schematic representation of the replacement of anodic OER with GOR during ammonia production using CuNi(1 : 2) S as a bifunctional electrocatalyst.

$C_6H_{10}O_7 + 2OH^- \rightarrow C_6H_{12}O_8 + 2H_2O + 2e^-$) is a potential candidate to pair with the NO_3RR to produce useful chemical commodities such as glucaric acid, gluconic acid and gluconolactone, used in polymer synthesis, the pharmaceutical industry, food and beverage production, and agriculture.[32–37] Glucaric acid (GRA) is known as a "top valuable compound" derived from biomass.[38] It serves as an essential intermediate in the production of biodegradable polymers, eco-friendly detergents, and metal chelating agents.[35,39] A market report from Grand View Research, Inc. indicates that the global GRA market size was approximately USD 550.4 million in 2016, with projections to reach USD 1.30 billion by 2025.[35] The substitution of the NO_3RR–OER pair with the NO_3RR–GOR pair in NO_3^- electrolysis could be a game changing strategy which provides value-added products in both anodic and cathodic reactions while simultaneously reducing the total energy demand required for efficient NH_3 production.[40–44] Designing a bifunctional catalyst for the NO_3RR and GOR is challenging, as it must facilitate both reactions with distinct mechanisms. Noble metals like Pt, Ru, Rh, and Pd are efficient but costly and scarce, prompting the search for earth-abundant, cost-effective alternatives.[40–46] Transition metal catalysts, particularly Cu-based ones, are promising for the NO_3RR to NH_3 due to the similar energies of the Cu d orbital and the π^* (LUMO) molecular orbital of NO_3.[47–50] Although Cu-based catalysts have weak proton adsorption, which minimizes the competitive HER, insufficient hydrogen adsorption species hinder intermediate (NO_2^-, NO, *etc.*) hydrogenation, which is critical for NH_3 formation.[47–50] Nickel (Ni) exhibits significant O–H activation and a strong affinity for the adsorption of hydrogen (H*) species.[51] Incorporating Ni into Cu-based catalysts optimizes the hydrogen species supply for nitrate reduction while minimizing the superfluous HER.[52] Additionally, Ni and Cu-based catalysts have shown notable success in electrochemical glucose oxidation.[53–55] Herein, we investigated a cost-effective transition metal-based bifunctional catalyst CuNi(1 : 2)S for glucose-assisted electrochemical nitrate reduction for ammonia production at room temperature (Fig. 1). The proposed catalyst demonstrated superior NO_3RR electrocatalytic activity for NH_3 production with a high NH_3 yield rate of 4.76 mg h^{-1} cm^{-2} and a F.E. of 93.44%. Under full cell conditions, the NH_3 yield rate improved from 120.95 μg h^{-1} cm^{-2} to 259.46 μg h^{-1} cm^{-2} in the presence of glucose.

Results and discussion

Synthesis and characterization

The CuNi(x : y)S catalyst along with the control catalysts, NiS and Cu_xS, were synthesized using a one-step hydrothermal method (detailed in the ESI†), and its microstructure was assessed using the powder X-ray diffraction (P-XRD) pattern. The P-XRD pattern (Fig. 2a) of the synthesized NiS demonstrated diffraction peaks at $2\theta = 30.168°$, 34.743° 46.035°, and 53.547°, which are attributed to the (100), (101), (102) and (110) planes of NiS matching with JCPDS no. 02-1280. Furthermore, the P-XRD pattern of Cu_xS revealed a combination of peaks that corresponded to CuS (JCPDS no. 06-0464) and Cu_2S (JCPDS no. 53-0522), with the most prominent peak at 31.785°, which can be attributed to the (103) plane of CuS and a major peak at 46.105° corresponding to the (220) plane of Cu_2S. Thus, the P-XRD pattern of the designed CuNi(x : y)S catalysts demonstrated the coexistence of NiS, CuS and Cu_2S in all the synthesised variants, matching well with their respective standard JCPDS data (Fig. 2a and S1†). CuNi(1 : 2)S, as revealed by the field emission scanning electron microscopy (FE-SEM) image,

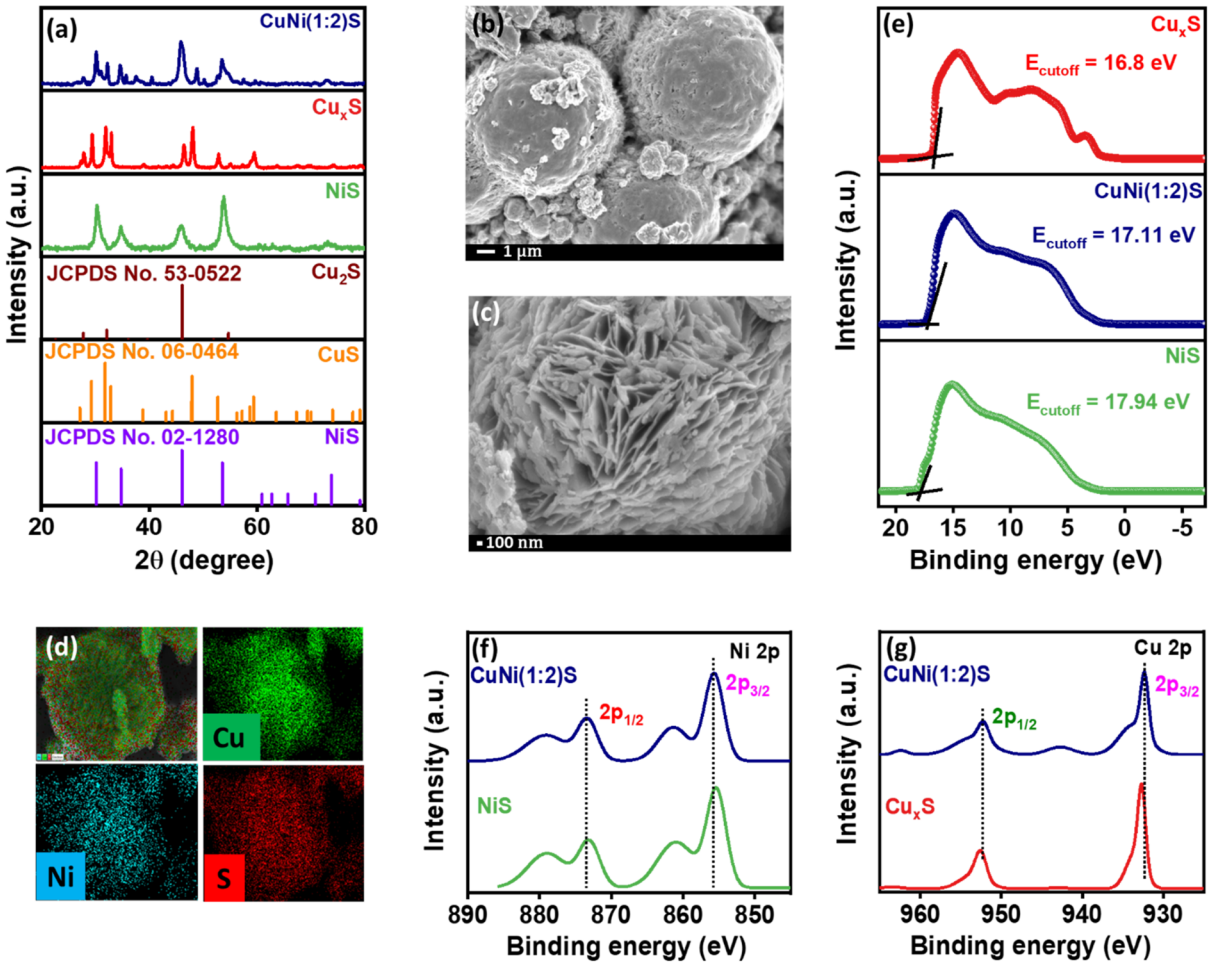

Fig. 2 (a) P-XRD pattern of NiS, Cu$_x$S, and CuNi(1 : 2)S catalysts, (b and c) FE-SEM at 1 μm and 100 nm magnification for the CuNi(1 : 2)S catalyst, and (d) elemental dot mapping showing the uniform distribution of Cu, Ni and S elements over the scanned area of CuNiS(1 : 2). (e) UPS spectra of Cu$_x$S, NiS and CuNi(1 : 2)S catalysts. Comparison of XPS spectra for (f) Ni 2p and (g) Cu 2p of CuNi(1 : 2)S with NiS and Cu$_x$S, respectively.

exhibited a spherical morphology wherein the flakes aggregated into microspheres (Fig. 2b and c). Similarly, NiS and Cu$_x$S showed a slightly distorted morphology with microspheres of varying sizes (Fig. S2†). In addition, energy dispersive X-ray spectroscopy (EDS) elemental dot mapping validated the coexistence and uniform distribution of Cu, Ni and S within the sphere (Fig. 2d). Besides, UPS was utilized to understand the interactions between NiS and Cu$_x$S in the CuNi(1 : 2)S catalyst. Fig. 2e reveals the secondary electron cutoff energy[56,57] (E_{cutoff}) at a binding energy (BE) of *ca.* 17.94 eV, 16.8 eV and 17.11 eV for NiS, CuS and CuNi(1 : 2)S, respectively. The work function (WF) of CuNi(1 : 2)S was computed to be 6.33 eV which lies between the WFs of NiS (5.8 eV) and CuS (6.59 eV) signifying electron transfer from Ni to Cu in the CuNi(1 : 2)S catalyst (Table S1, detailed calculation in the ESI†). Additionally, X-ray photoelectron spectroscopy (XPS) analysis was carried out to comprehend the oxidation states of the elements in the CuNi(1 : 2)S catalyst. The XPS survey spectrum shows the presence of all the expected elements Cu, Ni and S in the CuNi(1 : 2)S catalyst (Fig. S3a†). The deconvoluted Ni 2p XP spectra exhibited peaks at BEs of 873.3 eV and 855.65 eV, which are separated by 17.65 eV, corresponding to Ni 2p$_{1/2}$ and Ni 2p$_{3/2}$, respectively, with satellite peaks at 879.07 eV and 861.3 eV ascribed to Ni in the +2 oxidation state (Fig. S3b†).[58] The deconvoluted Cu 2p XPS pattern shown in Fig. S3c† revealed BE peaks at 932.3 eV and 952.2 eV corresponding to 2p$_{3/2}$ and 2p$_{1/2}$, respectively, of Cu^{+}. Furthermore, peaks at 933.67 eV and 953.48 eV correspond to 2p$_{3/2}$ and 2p$_{1/2}$ of Cu^{2+}.[59,60] Thus, we can conclude that Cu is present in both Cu(I) and Cu(II) oxidation states in the CuNi(1 : 2)S catalyst. Two satellite peaks were also observed at 942.72 eV and 962.42 eV, which are ascribed to Cu^{2+}.[59] Furthermore, the deconvoluted S 2p XP spectrum revealed peaks at 161.21 eV and 162.15 eV corresponding to S 2p$_{3/2}$ and S 2p$_{1/2}$ bonded with metal, while the peaks at 163.29 eV and 168.02 eV represented divalent sulphide and sulphate, respectively (Fig. S3d†).[61] Furthermore, the increase in BE of Ni 2p by 0.3 eV in CuNi(1 : 2)S and the decrease in BE of Cu 2p by 0.3 eV in CuNi(1 : 2)S relative to Cu$_x$S indicate successful Cu–Ni binding in CuNi(1 : 2)S (Fig. 2f and g). All the aforementioned observations from UPS and XPS indicate close chemical interaction between Cu and Ni, involving the transfer of electrons from Ni to Cu atoms within CuNi(1 : 2)S.[62–64]

Electrochemical nitrate reduction (NO_3RR)

The electrocatalytic activity of the designed CuNi(x : y)S catalysts towards the NO_3RR was investigated using various electrochemical and spectroscopic techniques. Initially, linear sweep voltammetric (LSV) experiments were conducted in Ar-saturated 1 M KOH + 100 mM KNO_3 (Fig. S4A†) at a scan rate of 25 mV s^{-1}. As observed in Fig. 3a, the reduction current was observed at a potential of −0.095 V, reaching the highest current density of 270 mA cm^{-2} @ −0.6 V *vs.* RHE. While a shift in the reduction current to more negative potentials was observed in the absence of KNO_3 signifying that the designed catalyst is active towards nitrate reduction. To gain a deeper understanding of the role of dual metal catalysts in NO_3RR activity, control experiments were performed using monometallic catalysts *viz.* NiS and Cu_xS. The comparison of LSV curves (Table S2†) for the synthesized monometallic catalysts *viz.* NiS and Cu_xS is shown in Fig. 3a. As expected, the onset potentials were observed at more negative values of −0.25 V and −0.22 for Cu_xS and NiS, respectively, which are higher than that of the CuNi(1 : 2)S catalyst (−0.095 V). The current density @ −0.6 V *vs.* RHE was found to be 194 mA cm^{-2} and 155 mA cm^{-2} for Cu_xS and NiS, respectively, both of which are lower than that of the CuNi(1 : 2)S catalyst indicating its superior NO_3RR activity. Hence, to understand the role of the Cu to Ni ratio in the CuNi(x : y)S catalyst, further experiments were performed with other variants. As observed in Fig. S4B,† the onset potential for CuNi(1 : 1)S and CuNi(2 : 1)S was almost similar which is −0.14 V *vs.* RHE, reaching current densities of 248 mA cm^{-2} and 237 mA cm^{-2} respectively @ −0.6 V *vs.* RHE. Furthermore, to quantify the ammonia produced during nitrate reduction, chronoamperometric measurements were conducted in an Ar-saturated 100 mM KNO_3 + 1 M KOH solution at various potentials ranging from −0.2 V to −0.6 V *vs.* RHE for 1 h each (Fig. 3b). The electrolyte was collected after 1 h of chronoamperometric electrolysis at different potentials and subjected to UV-Vis studies using the indophenol blue method (Fig. S5 and S6†). As observed in Fig. 3c, the NH_3 yield rate increased as the potential moved towards more negative values during the NO_3RR, indicating higher NH_3 synthesis at larger negative potential. The highest NH_3 yield rate of 8.05 mg h^{-1} cm^{-2} was attained at −0.6 V *vs.* RHE. Furthermore, the F.E. of NH_3 was calculated at various potentials, revealing 93.44% F.E. at −0.4 V *vs.* RHE with an NH_3 yield rate of 4.76 mg h^{-1} cm^{-2} (Fig. 3c) and a turn over frequency (TOF) of 11.92 h^{-1} suggesting the efficient performance of CuNi(1 : 2)S towards the NO_3RR to ammonia (Table S3†). The validation of generated NH_3 and reliability of the data for the same have emerged as critical and significant criteria. As a result, a strict methodology was followed, including cleaning of cell components.[65] Moreover, prior to the electrochemical experiments, the feeding Ar gas was passed through an alkaline $KMnO_4$ scrubbing solution to remove the impurities of reducible and labile N-containing compounds, namely NO_x.[66] The use of Ni foam as a substrate for the working electrode was mainly due to its higher surface area and high conductivity.[67] Meanwhile, it has been proven that Ni foam is a relatively inert material for the NO_3RR, while maintaining the catalyst's performance.[67,68] Thus, similar control experiments were performed on the bare Ni foam electrode at −0.4 V *vs.* RHE and in the absence of NO_3^- using CuNi(1 : 2)S. As can be seen in the UV-Vis spectra (Fig. 3d) negligible absorbance was observed in

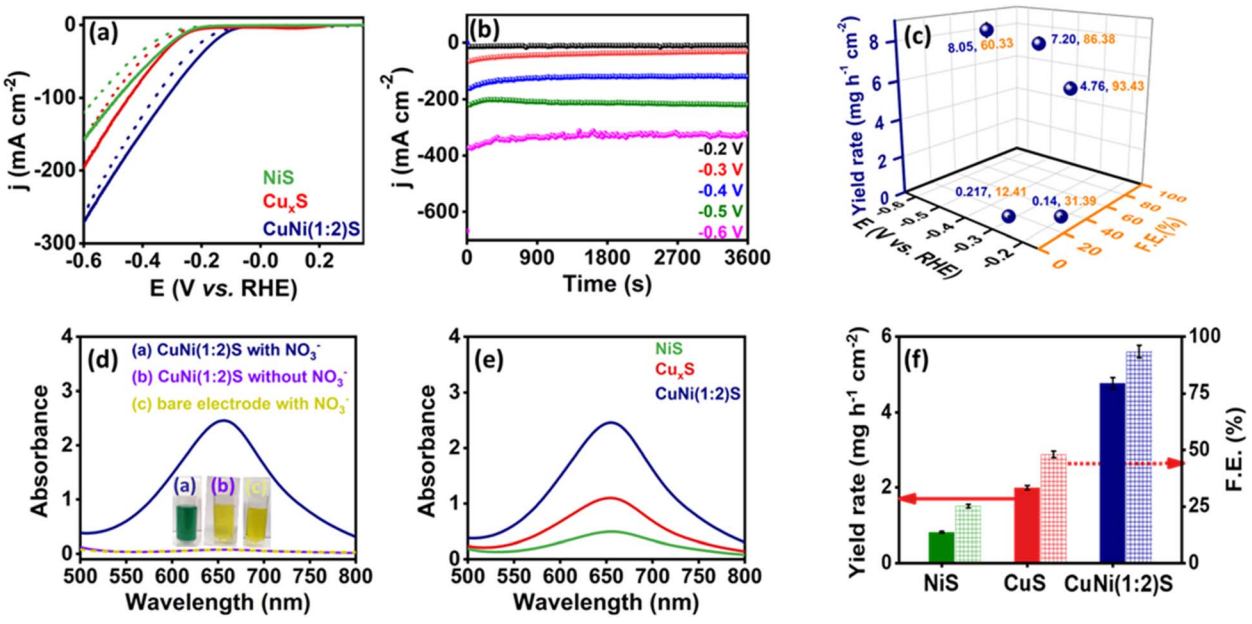

Fig. 3 (a) LSV for NiS, Cu_xS and CuNi(1 : 2)S catalysts in Ar saturated 1 M KOH solution in the presence (solid line) and absence (dashed line) of 100 mM KNO_3, (b) chronoamperometric curves for the CuNi(1 : 2)S catalyst in Ar saturated 1 M KOH in the presence of 100 mM KNO_3 at different potentials and (c) graph representing the corresponding NH_3 yield rate and F.E. (d) UV-Vis spectra obtained by the indophenol blue method for CuNi(1 : 2)S under various conditions and (e) comparison of UV-Vis spectra of NiS, Cu_xS and CuNi(1 : 2)S at −0.4 V *vs.* RHE. (f) Bar diagram representing the corresponding NH_3 yield rate and F.E. (WE: Ni foam; RE: Hg/HgO/1 M NaOH; CE: graphite rod).

both the cases and the quantification clearly indicates that a negligible amount of NH_3 was produced (Fig. S7†). Thus, it is affirmed that the source of NH_3 is exclusively from the added NO_3^- and there are no potential interferences. Furthermore monometallic variants (NiS and Cu_xS) were also compared with CuNi(1 : 2)S under similar experimental conditions (Fig. 3e and S8†). It was observed that CuNi(1 : 2)S exhibited a considerably enhanced NH_3 yield rate (4.76 mg h^{-1} cm^{-2}) and F.E. (93.44%) compared to monometallic NiS (0.81 μg h^{-1} cm^{-2}, 25.02%) and Cu_xS (2.00 mg h^{-1} cm^{-2}, 48.02%) at a potential of −0.4 V *vs.* RHE (Fig. 3f). The superior performance of CuNi(1 : 2)S benefited from the advantageous synergy between Cu and Ni in CuNi(1 : 2)S. More importantly, all the three variants of CuNi(*x* : *y*)S with different metal ratios exhibited a high F.E. of more than 80%, with CuNi(1 : 2)S showing the highest NH_3 yield rate and F.E., indicating its superior NO_3RR activity (Fig. S9†). This superior activity of CuNi(1 : 2)S was further justified by various electrochemical characterization techniques including Tafel analysis, electrochemical impedance spectroscopy (EIS) and electrochemical surface area (ECSA) analysis. First, the Tafel slopes were obtained from LSV curves shown in Fig. 3a for the catalysts in the presence of NO_3^-. The lower Tafel slope of 102 mV dec^{-1} for CuNi(1 : 2)S as compared to other controlled synthesized catalyst variants (Fig. S8b, S10 and Table S4†), indicated its faster kinetics towards the NO_3RR. Furthermore, the Tafel slope slightly less than 120 mV dec^{-1} signifies that the rate determining step is the first one electron transfer that occurs during the NO_3^- to NO_2^- conversion.[69,70] Furthermore, to confirm the conclusions from Tafel analysis, electrochemical impedance spectroscopic (EIS) analysis was conducted by recording Nyquist plots at −0.4 V in the presence of NO_3^- over the frequency range of 7 mHz to 3 MHz. As shown in Fig. S11,† a lower charge transfer resistance (R_{ct}) was observed for CuNi(1 : 2)S (Table S5†), signifying a fast charge transfer at the electrode–electrolyte interface during the electrochemical reaction. To further validate this, we estimated the exchange current density and rate constant from the R_{ct} values using the following equations.[71–73]

$$R_{ct} = RT/nFi_0 \quad (1)$$

$$R_{ct} = RT/n^2F^2Ack_0 \quad (2)$$

where, R_{ct} is the charge transfer resistance, R is the universal gas constant, T is the temperature, n is the number of electrons, F is Faraday's constant, i_0 is the exchange current density, A is the surface area, c is the concentration, and k_0 is the rate constant. The i_0 and k_0 values were determined to be 3.55 mA cm^{-2} and 5.78×10^{-9} cm s^{-1}, respectively, for the CuNi(1 : 2)S catalyst. These values are higher than those for Cu_xS (2.80 mA cm^{-2}, 4.56 cm s^{-1}) and NiS (2.72 mA cm^{-2}, 4.43×10^{-9} cm s^{-1}), indicating an enhanced rate of reaction. Furthermore, the i_0 and k_0 values for CuNi(1 : 1)S and CuNi(2 : 1)S catalysts were found to be 3.48 mA cm^{-2}, 5.67×10^{-9} cm s^{-1} and 3.34 mA cm^{-2}, 5.44×10^{-9} cm s^{-1} respectively. This facile kinetics could also be attributed to the increased number of accessible electrochemically active sites on the catalyst surface, as measured using the double layer capacitance (C_{dl}) in the non-faradaic region. The electrochemical surface area (ECSA) of the CuNi(1 : 2)S catalyst was found to be 37.5 cm^2 which is superior to that of other variants (Fig. S12 and Table S6†). Thus, the superior activity of the CuNi(1 : 2)S catalyst towards the NO_3RR was substantially justified by its lower charge transfer resistance (R_{ct}) and higher ECSA.

To confirm that the ammonia generated herein is a result of the NO_3RR only, the most consistent control isotope labelling experiments were performed using $^{14}NO_3^-$ and $^{15}NO_3^-$ potassium salts as the N source (Fig. 4a). For the quantitative analysis of $^{15}NH_4^+/^{14}NH_4^+$ acquired from the isotope labelling studies, the calibration curves were extracted for different known concentrations of $^{14}NH_4^+$ and $^{15}NH_4^+$ using ^{1}H NMR spectra (Fig. S13 and S14†). After electrolysis of the $^{14}NO_3^-$ aqueous solution, ^{1}H NMR spectra were acquired exhibiting a triplet with peaks present at 7.06, 6.93 and 6.8 ppm corresponding to a coupling constant of ∼52 Hz, which were attributed to $^{14}NH_4^+$ signals. On the other hand, the ^{1}H NMR spectrum of the $^{15}NO_3^-$ aqueous solution upon electrolysis showed a doublet at 7.02 and 6.84 ppm with a coupling constant of ∼72 Hz and no doublet or triplet was observed in the absence of NO_3^-, indicating that the chemical origin of the produced NH_3 during the NO_3RR is due to the supplied NO_3^- (Fig. 4a). Quantification of NH_3 for both $^{15}NH_4^+$ and $^{14}NH_4^+$ obtained by ^{1}H NMR is consistent with the indophenol blue method (Fig. 4b and Table S7†). Similarly, quantification of NH_3 produced by the electrochemical NO_3RR using the CuNi(1 : 2)S catalyst was further validated by Nessler's reagent test and Fig. 4c shows almost similar NH_3 yield values obtained from all the three methods (Fig. 4c, S15 and Table S8†).

To corroborate whether any intermediate/by products *viz.*, nitrites (NO_2^-), hydrazine (N_2H_4), and hydroxyl amine (NH_2OH) were produced during the NO_3RR, they were also quantified after chronoamperometric analysis under similar experimental conditions. NO_2^- was quantified using the Griess method[74] at potentials similar to those used for NH_3 quantification and it was found that a maximum F.E. of 6.52% was achieved at −0.4 V *vs.* RHE (Fig. S16 and S17†).

Furthermore, N_2H_4 and NH_2OH by products were also quantified using various colorimetric and UV-Vis spectroscopy techniques (Fig. S18 and S19 detailed in the ESI†). It is worth noting that N_2H_4 and NH_2OH were not detected as revealed by the UV-Vis spectra (Fig. S18c and S19c†), thus indicating a relatively high selectivity for NH_3 synthesis by CuNi(1 : 2)S. The total F.E. for the NO_3RR at a potential of −0.4 V *vs.* RHE was found to be 99.96% (∼100%) with the F.E. for NH_3, and NO_2^- being 93.44% and 6.52%, respectively (Fig. S20†). The energy efficiency was found to be 30.95% at a potential of −0.4 V *vs.* RHE (details in ESI†).

This was further confirmed by *in situ* electrochemical Raman spectroscopy (Fig. 4d). The Raman spectra was recorded over the range of 980 to 1600 cm^{-1} under an applied potential of −0.4 V *vs.* RHE. Initially, the only prominent peak was observed at around 1043 cm^{-1}, which is attributed to the presence of nitrate ions (NO_3^-).[67] As the electrochemical reaction progressed, a new peak emerged at approximately 1056 cm^{-1},

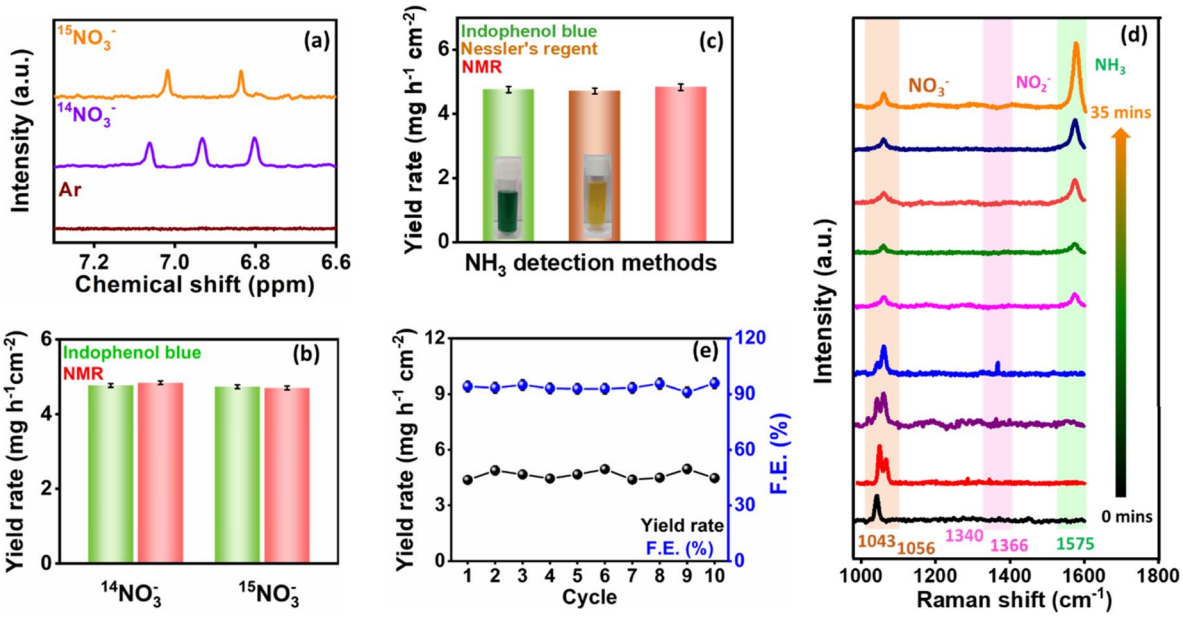

Fig. 4 (a) ^{1}H NMR spectra obtained after the NO_3RR for CuNi(1 : 2)S in Ar saturated, $^{14}NO_3^-$-, and $^{15}NO_3^-$-containing electrolyte solutions. A bar diagram representing the comparison of the NH_3 yield calculated from calibrated data by the (b) indophenol method, and NMR for $^{14}NH_4^+$ and $^{15}NH_4^+$ produced during the NO_3RR, and (c) $^{14}NH_3$ detection by the indophenol blue method, Nessler's reagent test and NMR. (d) Time dependent *in situ* electrochemical Raman spectra of the CuNi(1 : 2)S catalyst at −0.4 V *vs.* RHE. (e) NH_3 yield and F.E. for consecutive 10 cycles at −0.4 V *vs.* RHE using the CuNi(1 : 2)S catalyst.

corresponding to the stretching vibrations of the NO_3^- ions.[75] This suggests the formation of an intermediate or a slight change in the chemical environment of the NO_3^- ions, indicating NO_3^- reduction. Additionally, peaks at 1340 cm^{-1} and 1366 cm^{-1} were observed at the onset of the reaction in the measurements, representing symmetric and antisymmetric stretching of NO_2 in NO_3^-, respectively.[76,77] This indicates the reduction of NO_3^- *via* NO_2. As the reaction time increases, the intensity of the peak corresponding to NO_3^- (initially at 1043 cm^{-1}) decreases, indicating the consumption or transformation of nitrate ions during the reduction process. Simultaneously, a new peak emerges at around 1575 cm^{-1}. This peak is attributed to the antisymmetric bending vibrations of the HNH moiety in ammonia (NH_3).[67,78] The increasing intensity of this peak over time suggests a greater formation of ammonia as the reaction progresses. Thus, the Raman spectral changes observed during the electrochemical nitrate reduction provide insights into the formation of intermediate species and the conversion of nitrate ions to ammonia. Thus, based on our electrochemical results and previous studies, we conclude that the electrochemical reaction $NO_3^- + 6H_2O + 8e^- \rightarrow NH_3 + 9OH^-$ is characterized by a sequence of deoxidation reactions ($*NO_3^- \rightarrow *NO_2 \rightarrow *NO \rightarrow *N$), followed by hydrogenation steps ($*N \rightarrow *NH \rightarrow *NH_2 \rightarrow *NH_3$).[25,79]

Along with electrochemical activity, stability is an important parameter for evaluating the performance of catalyst. The electrochemical stability of CuNi(1 : 2)S towards the NO_3RR was then investigated through electrolysis for 10 consecutive cycles (1 h each) at the potential of −0.4 V *vs.* RHE. The chronoamperometric curves revealed a negligible change in the current response and the corresponding UV-Vis spectra for consecutive 10 cycles of 1 h each remained consistent (Fig. S21†). A steady F.E. and NH_3 yield were maintained throughout the 10-h stability test (Fig. 4e). Moreover, post analysis of the catalyst after prolonged chronoamperometric measurement was further investigated by P-XRD, FE-SEM and XPS. The P-XRD pattern and FE-SEM image showed that the crystalline structure and morphology are well preserved (Fig. S22a and b†). Furthermore, post XPS analysis (Fig. S23†) showed no change in the chemical composition of elements present in CuNi(1 : 2)S confirming the high stability of the catalyst towards the NO_3RR. The aforementioned results show the appreciable activity and robust nature of CuNi(1 : 2)S towards the NO_3RR in alkaline media and its superiority compared to the reported literature (Table S9†).

Glucose oxidation reaction (GOR)

To probe the catalytic activity of CuNi(x : y)S towards the glucose oxidation reaction (GOR), LSV curves were recorded for all variants in the absence (*i.e.*, OER) and presence of glucose (*i.e.*, GOR) in 1 M KOH at a scan rate of 5 mV s^{-1} in a 3-electrode assembly, with catalyst-coated Ni foam serving as the working electrode (WE), graphite rod as the counter electrode (CE), and Hg/HgO/1 M NaOH as the reference electrode (RE). The catalyst was activated prior to the LSV measurements by recording cyclic voltammetry patterns at a scan rate of 50 mV s^{-1} for 50 cycles. Cyclic voltammetry patterns in Fig. S24† illustrate the behaviour of CuNi(1 : 2)S for 50 cycles in 1 M KOH where both the anodic and cathodic peak current displayed an exponential increase in the current w.r.t cycles, indicating the formation of a metal oxide layer. The plausible mechanism involved in the GOR is as

follows: Cu and Ni atoms are initially oxidised and then they take part in the GOR as described by reactions (3) and (4):[55]

$$NiO + CuO + 2OH^- \rightarrow NiO(OH) + CuO(OH) + 2e^- \quad (3)$$

$$NiO(OH) + CuO(OH) + 2\ glucose \rightarrow NiO + CuO + 2\ glucose_{ox} \quad (4)$$

Among the several variants of synthesised catalysts examined, CuNi(1 : 2)S exhibited the highest GOR activity, with an onset potential of 1.35 V *vs.* RHE as observed in Fig. 5a and S25.† The comparison of LSV for OER and GOR activity of CuNi(1 : 2)S in Fig. 5a depicts that the GOR occurs at a lower potential of 1.35 V *vs.* RHE as compared to the OER (1.55 V *vs.* RHE). In addition, a lower Tafel slope value of 78 mV dec^{-1} in the presence of glucose was obtained, compared to that for OER (146 mV dec^{-1}) for CuNi(1 : 2)S (Fig. S26†), pointed towards faster kinetics for glucose oxidation in comparison to oxygen evolution.[31] To determine the precise onset potential for the GOR, sequential chronoamperometric measurements were performed at potentials ranging from 1.1 V to 1.6 V *vs.* RHE with a 0.05 V interval for 4 minutes each. As shown in Fig. S27,† the current density showed a sudden increase for the GOR at 1.35 V *vs.* RHE, whereas for the OER, the current density increased only after 1.55 V *vs.* RHE. Furthermore, the catalytic performance of CuNi(1 : 2)S was assessed by recording LSV curves across various concentrations from 0 to 250 mM (Fig. S28†). Interestingly, an increasing trend in current density was observed up to 100 mM glucose concentration and upon further increasing the glucose concentration, a decline in current density was observed which could be potentially attributed to the attainment of complete coverage of the catalyst surface by glucose.[31] Furthermore, to examine the products obtained during the GOR, chronopotentiometry measurement at 50 mA cm^{-2} was performed for 4 h (Fig. 5b) and the electrolyte was analysed using high resolution mass spectrometry (HRMS, Fig. S29†). Table S10† depicts the successful formation of gluconic acid, glucaric acid, guluronic acid and their adducts. Moreover, long-term chronopotentiometry tests were performed at 50 and 100 mA cm^{-2} for 15 h, displaying good stability of the catalyst with a negligible decrease in current density (Fig. S30†). Table S11† shows the comparable performance of our catalyst to that reported in the literature. Thus, CuNi(1 : 2)S demonstrates remarkable bifunctional activity towards the electrocatalytic NO_3RR and GOR for the production of value added products from both reactions.

Glucose oxidation assisted NH_3 production

The outstanding bifunctional catalytic activity of CuNi(1 : 2)S towards both the cathodic NO_3RR and anodic GOR, inspired us to investigate its practical applicability for glucose oxidation assisted NH_3 generation. We assembled a full cell using CuNi(1 : 2)S as both the anode and cathode electrocatalysts in a homemade H-type cell separated by a Nafion membrane. The anodic chamber was filled with a solution of 1 M KOH + 100 mM glucose. On the other hand, the cathodic chamber was filled with a solution containing 1 M KOH + 100 mM KNO_3, to facilitate the reduction of nitrate. Initially the LSV curve was recorded in the presence of glucose, which showed an increase in the current density at a potential of 1.25 V, whereas a voltage of 1.45 V was observed in the absence of glucose, which is 200 mV higher (Fig. 5d). Moreover, the NO_3RR–OER cell configuration

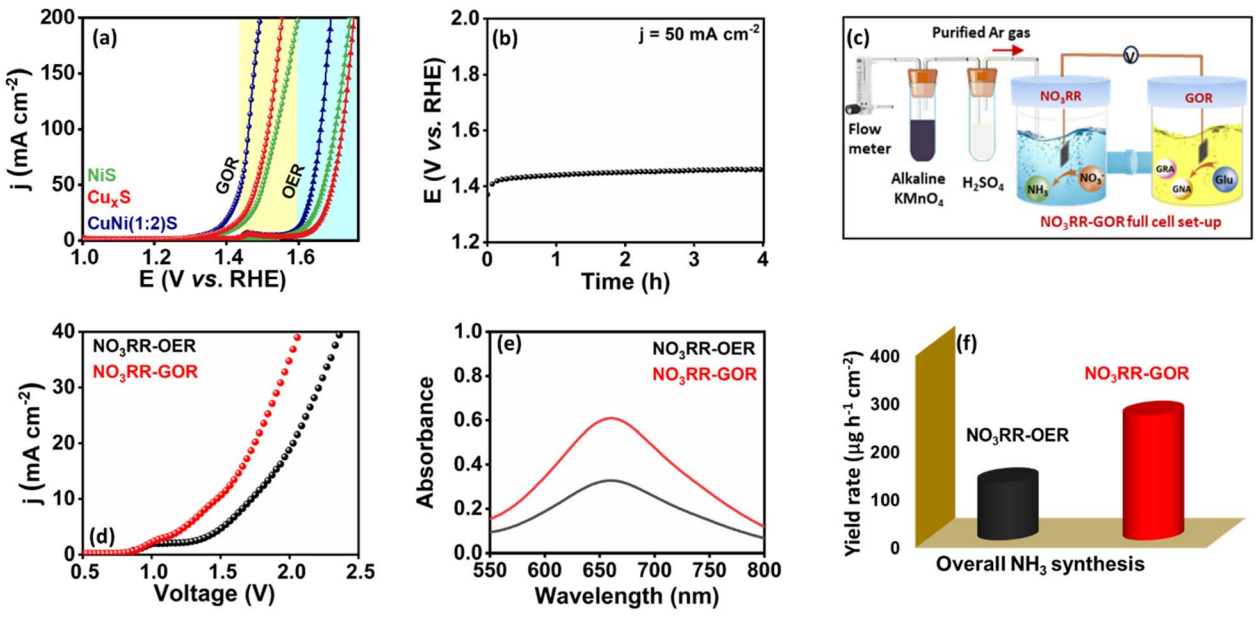

Fig. 5 (a) LSV for the GOR and OER for NiS, Cu_xS, and CuNi(1 : 2)S at a scan rate of 5 mV s^{-1}, (b) chronopotentiometry measurement at 50 mA cm^{-2} for glucose oxidation, and (c) Schematic representation for the gas-purification set-up during the NO_3RR–GOR full cell experiment for purification of the gas-supply. (d) Comparison of LSV for NO_3RR–OER and NO_3RR–GOR for full cell studies, and (e) UV-Vis spectra after chronoamperometry at a potential of 1.5 V in the absence and presence of glucose and (f) bar diagram showing the NH_3 yield rate in NO_3RR–OER and NO_3RR–GOR after electrolysis at 1.5 V.

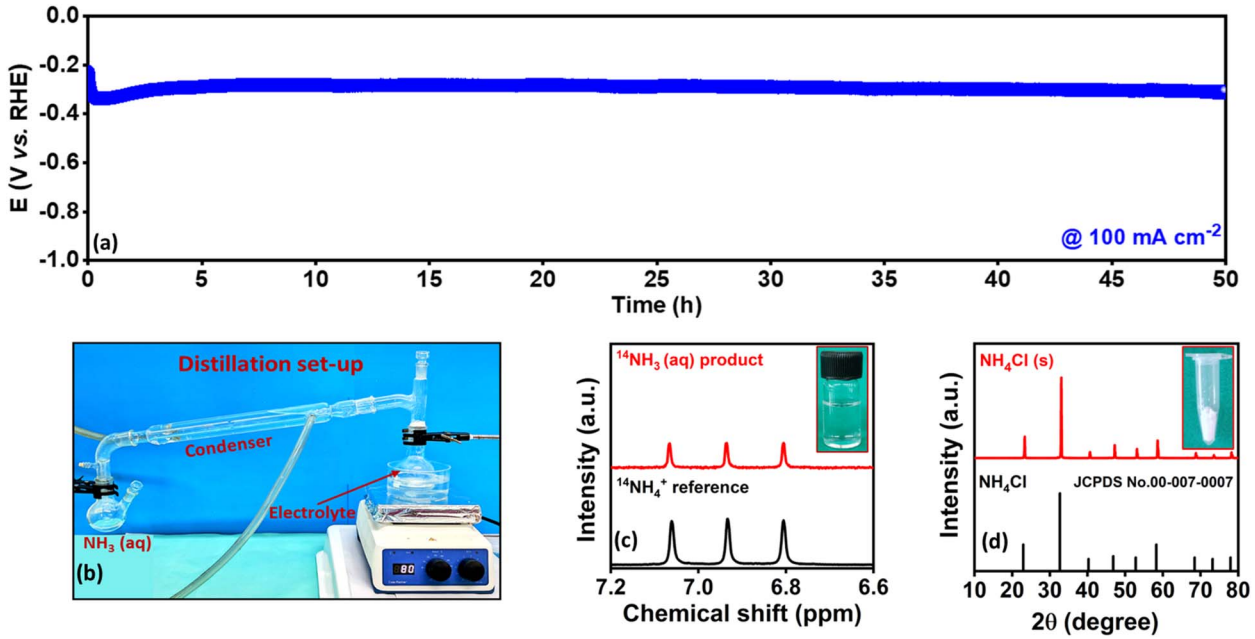

Fig. 6 (a) Chronopotentiometry of CuNi(1 : 2)S at 100 mA cm^{-2} in 1 M KOH with 100 mM KNO_3 for 50 h and (b) photograph showing the distillation set-up for the extraction of condensed NH_3(aq) from the electrolyte solution after 50 h of electrolysis. (c) ^1H NMR spectra with the inset showing the photograph of condensed NH_3(aq) and (d) XRD pattern with the inset showing the photograph of the extracted NH_4Cl(s).

requires a voltage of 1.72 V to reach a current density of 10 mA cm^{-2}. However, when the OER is substituted with the GOR at the anode during NH_3 production, a voltage of 1.48 V is enough to accomplish the same current density. After electrolysis for 1 h at a potential of 1.5 V, a further evaluation of the NH_3 generation yield was carried out using UV-Vis spectroscopy (Fig. S31† and 5e). The NH_3 yield rate of 259.46 μg h^{-1} cm^{-2} for the NO_3RR–GOR cell was determined, which is higher than the NH_3 yield rate for the NO_3RR–OER cell system (120.95 μg h^{-1} cm^{-2}), as shown in Fig. 5f. This strengthens the relevance of our conceptualization. Therefore, this work may delve into the implementation of metal sulphides for overall NH_3 production at decreased cell voltage by substituting the anodic OER with GOR for practical application.

Extraction of pure ammonia

With our catalyst's noteworthy NO_3RR performance, we further illustrate the practical recovery of high-purity ammonia products. A catalyst's good stability is essential at industrially relevant current densities for real applications. Thus, we performed a long-term chronopotentiometry (CP) stability test of CuNi(1 : 2)S in an H-cell at a current density of 100 mA cm^{-2} for 50 h for the NO_3RR (Fig. 6a). After that, ammonia was extracted from the electrolyte solution *via* the distillation process, which resulted in ammonia condensation in the receiver flask while leaving the remaining reaction mixture in the distilling flask (Fig. 6b and Scheme S1, detailed in the ESI†). The condensed NH_3(aq) was verified using ^1H NMR spectroscopy as shown in Fig. 6c and the inset shows the condensed NH_3. The condensed NH_3 was quantified by UV-Vis spectroscopy, with a condensation collection efficiency of 89.84% (detailed in the ESI†). The condensed NH_3(aq) solution was further treated with HCl to finally form NH_4Cl.[80] High-purity NH_4Cl(s) powder was obtained through rotary evaporation at a temperature of 40 °C, and its formation was confirmed by the XRD pattern that matches with standard JCPDS ICDD no. 00-007-0007, with no extra peak (Fig. 6d). The collection efficiency of solid NH_4Cl was also calculated to be 82.27%. This practical illustration shows the entire process for electrochemically converting nitrate to an advantageous, high-purity ammonia product.

Conclusion

In summary, we successfully synthesised a CuNi binary metal sulphide CuNi(x : y)S catalyst using a one-step hydrothermal approach with flakes aggregated into a microsphere-like morphology for the glucose assisted NO_3RR in alkaline media. A high NH_3 yield of 4.76 mg h^{-1} cm^{-2} (280.47 mmol g_{cat}^{-1} h^{-1}) and a F.E. of 93.44% at a potential of −0.4 V (*vs.* RHE) with a high current density of ∼118 mA cm^{-2} was achieved for the CuNi(1 : 2)S catalyst, which is superior to the yield obtained in the industrial Haber–Bosch process (<200 mmol g_{cat}^{-1} h^{-1}).[40] Moreover, the successful NO_3RR to NH_3 conversion was studied by *in situ* electrochemical Raman spectroscopy. The full-cell studies reveal 2.14 times higher NH_3 yield for the NO_3RR–GOR system compared to the NO_3RR–OER system. This work unveils the synergistic effect of Cu and Ni for efficient NO_3RR and GOR and contributes to a better understanding and design of effective bimetallic catalysts for the NO_3RR and other applications. This study significantly broadens the area of research for the glucose-assisted NH_3 generation at lower cell potential with high NH_3 yield, which is accomplished by substituting the sluggish oxygen evolution reaction with the GOR. Furthermore,

we extracted a pure NH_3 aqueous product and NH_4Cl for large-scale industrial application.

Data availability

The data supporting this article have been included as part of the ESI.†

Conflicts of interest

There are no conflicts to declare.

Acknowledgements

T. C. Nagaiah thanks the Science and Engineering Research Board (SERB, CRG/2018/004478 and SPG/2021/002415) for funding. A. Chaturvedi acknowledges I.I.T Ropar for the fellowship and research facilities. S. K. thanks the CSIR (09/1005(0029)/2020-EMR-1) for the fellowship. K. G. acknowledges the Prime Minister Research Fellowship (PMRF) scheme for a fellowship. We also thank the team at the Central Research Facility of I.I.T Ropar for the NMR and HRMS facilities and the department's LCMS facility (SR/FST/CS-I/2018/55).

Notes and references

1 J. Zhu, L. Hu, P. Zhao, L. Y. S. Lee and K.-Y. Wong, *Chem. Rev.*, 2020, **120**, 851–918.
2 R. Lan and S. Tao, *Front. Energy Res.*, 2014, **2**, 35.
3 D. Gupta, A. Kafle and T. C. Nagaiah, *Faraday Discuss.*, 2023, **243**, 339–353.
4 G. Qing, R. Ghazfar, S. T. Jackowski, F. Habibzadeh, M. M. Ashtiani, C.-P. Chen, M. R. Smith and T. W. Hamann, *Chem. Rev.*, 2020, **120**, 5437–5516.
5 V. Smil, *Nature*, 1999, **400**, 415.
6 A. Klerke, C. H. Christensen, J. K. Nørskov and T. Vegge, *J. Mater. Chem.*, 2008, **18**, 2304–2310.
7 R. Schlögl, *Angew. Chem., Int. Ed.*, 2003, **42**, 2004–2008.
8 C. Zamfirescu and I. Dincer, *J. Power Sources*, 2008, **185**, 459–465.
9 M. S. Allahyari and M. Sadeghzadeh, in *Zero Hunger*, ed. W. Leal Filho, A. M. Azul, L. Brandli, P. G. Özuyar and T. Wall, Springer International Publishing, Cham, 2020, pp. 41–52, DOI: 10.1007/978-3-319-95675-6_2.
10 S. Ahmad, L. Tang, R. Shahzad, A. M. Mawia, G. S. Rao, S. Jamil, C. Wei, Z. Sheng, G. Shao, X. Wei, P. Hu, M. M. Mahfouz, S. Hu and S. Tang, *J. Agric. Food Chem.*, 2021, **69**, 8307–8323.
11 G. Soloveichik, *Nat. Catal.*, 2019, **2**, 377–380.
12 G. Leigh, in *Catalysts for Nitrogen Fixation*, Springer, 2004, pp. 33–54.
13 S. Ghavam, M. Vahdati, I. Wilson and P. Styring, *Front. Energy Res.*, 2021, **9**, 34.
14 J. Nørskov, J. Chen, R. Miranda, T. Fitzsimmons and R. Stack, *Sustainable Ammonia Synthesis–Exploring the Scientific Challenges Associated with Discovering Alternative, Sustainable Processes for Ammonia Production*, US DOE Office of Science, 2016.
15 Y. Li, L. Ouyang, J. Chen, X. Fan, H. Sun, X. He, D. Zheng, S. Sun, Y. Luo, Q. Liu, L. Li, W. Chu, J. Du, Q. Kong, B. Zheng and X. Sun, *J. Colloid Interface Sci.*, 2024, **663**, 405–412.
16 C. Ma, L. Bao, X. Fan, X. He, X. Liu, W. Chu, A. Farouk, M. S. Hamdy, S. Sun, Q. Li, M. Wu and X. Sun, *Catal. Sci. Technol.*, 2024, **14**, 3007–3011.
17 C. S. Diercks, Y. Liu, K. E. Cordova and O. M. Yaghi, *Nat. Mater.*, 2018, **17**, 301–307.
18 F. Chang, W. Gao, J. Guo and P. Chen, *Adv. Mater.*, 2021, **33**, 2005721.
19 B. H. R. Suryanto, C. S. M. Kang, D. Wang, C. Xiao, F. Zhou, L. M. Azofra, L. Cavallo, X. Zhang and D. R. MacFarlane, *ACS Energy Lett.*, 2018, **3**, 1219–1224.
20 C. J. van der Ham, M. T. Koper and D. G. Hetterscheid, *Chem. Soc. Rev.*, 2014, **43**, 5183–5191.
21 Y. Luo, G.-F. Chen, L. Ding, X. Chen, L.-X. Ding and H. Wang, *Joule*, 2019, **3**, 279–289.
22 X. Cui, C. Tang and Q. Zhang, *Adv. Energy Mater.*, 2018, **8**(22), 1800369.
23 C. Guo, J. Ran, A. Vasileff and S.-Z. Qiao, *Energy Environ. Sci.*, 2018, **11**, 45–56.
24 D. Gupta, A. Kafle, S. Kaur and T. C. Nagaiah, *J. Mater. Chem. A*, 2023, **11**, 22132–22146.
25 Y. Wang, A. Xu, Z. Wang, L. Huang, J. Li, F. Li, J. Wicks, M. Luo, D.-H. Nam, C.-S. Tan, Y. Ding, J. Wu, Y. Lum, C.-T. Dinh, D. Sinton, G. Zheng and E. H. Sargent, *J. Am. Chem. Soc.*, 2020, **142**, 5702–5708.
26 S. Ye, Z. Chen, G. Zhang, W. Chen, C. Peng, X. Yang, L. Zheng, Y. Li, X. Ren, H. Cao, D. Xue, J. Qiu, Q. Zhang and J. Liu, *Energy Environ. Sci.*, 2022, **15**, 760–770.
27 X. Fan, J. Liang, L. Zhang, D. Zhao, L. Yue, Y. Luo, Q. Liu, L. Xie, N. Li, B. Tang, Q. Kong and X. Sun, *Carbon Neutralization*, 2022, **1**, 6–13.
28 X. Fan, C. Liu, X. He, Z. Li, L. Yue, W. Zhao, J. Li, Y. Wang, T. Li, Y. Luo, D. Zheng, S. Sun, Q. Liu, L. Li, W. Chu, F. Gong, B. Tang, Y. Yao and X. Sun, *Adv. Mater.*, 2024, **36**, 2401221.
29 X. He, T. Xie, K. Dong, J. Nan, H. Sun, Y. Yao, X. Fan, D. Zheng, Y. Luo, S. Sun, Q. Liu, L. Li, W. Chu, L. Xie, Q. Kong and X. Sun, *Sci. China Mater.*, 2024, DOI: 10.1007/s40843-024-2798-5.
30 Z. Lu, J. Wang, S. Huang, Y. Hou, Y. Li, Y. Zhao, S. Mu, J. Zhang and Y. Zhao, *Nano Energy*, 2017, **42**, 334–340.
31 N. Thakur, D. Mehta, A. Chaturvedi, D. Mandal and T. C. Nagaiah, *J. Mater. Chem. A*, 2023, **11**, 15868–15877.
32 A. Chaturvedi, D. Gupta, S. Kaur, K. Garg and T. C. Nagaiah, *J. Mater. Chem. A*, 2023, **11**, 18280–18290.
33 G. Chen, X. Li and X. Feng, *Angew. Chem., Int. Ed.*, 2022, **61**, e202209014.
34 M. Besson, P. Gallezot and C. Pinel, *Chem. Rev.*, 2014, **114**, 1827–1870.
35 W.-J. Liu, Z. Xu, D. Zhao, X.-Q. Pan, H.-C. Li, X. Hu, Z.-Y. Fan, W.-K. Wang, G.-H. Zhao and S. Jin, *Nat. Commun.*, 2020, **11**, 1–11.

36 Y. Zhang, B. Zhou, Z. Wei, W. Zhou, D. Wang, J. Tian, T. Wang, S. Zhao, J. Liu, L. Tao and S. Wang, *Adv. Mater.*, 2021, **33**, 2104791.
37 A. Chaturvedi, S. Gaber, S. Kaur, K. C. Ranjeesh, T. C. Nagaiah and D. Shetty, *ACS Energy Lett.*, 2024, **9**, 2484–2491.
38 A. J. Ragauskas, C. K. Williams, B. H. Davison, G. Britovsek, J. Cairney, C. A. Eckert, W. J. Frederick, J. P. Hallett, D. J. Leak, C. L. Liotta, J. R. Mielenz, R. Murphy, R. Templer and T. Tschaplinski, *Science*, 2006, **311**, 484–489.
39 A. Kardan, N. Ashraf, Z. Dabirifar and S. Khadempir, *RSC Adv.*, 2021, **11**, 10615–10624.
40 J. Li, G. Zhan, J. Yang, F. Quan, C. Mao, Y. Liu, B. Wang, F. Lei, L. Li, A. W. M. Chan, L. Xu, Y. Shi, Y. Du, W. Hao, P. K. Wong, J. Wang, S.-X. Dou, L. Zhang and J. C. Yu, *J. Am. Chem. Soc.*, 2020, **142**, 7036–7046.
41 J. Lim, C.-Y. Liu, J. Park, Y.-H. Liu, T. P. Senftle, S. W. Lee and M. C. Hatzell, *ACS Catal.*, 2021, **11**, 7568–7577.
42 Y. Han, X. Zhang, W. Cai, H. Zhao, Y. Zhang, Y. Sun, Z. Hu, S. Li, J. Lai and L. Wang, *J. Colloid Interface Sci.*, 2021, **600**, 620–628.
43 G. E. Dima, G. L. Beltramo and M. T. M. Koper, *Electrochim. Acta*, 2005, **50**, 4318–4326.
44 H.-F. Cui, J.-S. Ye, X. Liu, W.-D. Zhang and F.-S. Sheu, *Nanotechnology*, 2006, **17**, 2334.
45 Z. Tang, Z. Bai, X. Li, L. Ding, B. Zhang and X. Chang, *Processes*, 2022, **10**, 751.
46 J. Wang, Y. Wang, C. Cai, Y. Liu, D. Wu, M. Wang, M. Li, X. Wei, M. Shao and M. Gu, *Nano Lett.*, 2023, **23**, 1897–1903.
47 H. Xu, Y. Ma, J. Chen, W.-x. Zhang and J. Yang, *Chem. Soc. Rev.*, 2022, **51**, 2710–2758.
48 M. Teng, J. Ye, C. Wan, G. He, H. J. I. Chen and E. C. Research, *J. Ind. Eng. Chem.*, 2022, **61**, 14731–14746.
49 J. Zhao, L. Liu, Y. Yang, D. Liu, X. Peng, S. Liang and L. Jiang, *ACS Sustain. Chem. Eng.*, 2023, **11**, 2468–2475.
50 Y. Xu, K. Ren, T. Ren, M. Wang, Z. Wang, X. Li, L. Wang and H. Wang, *Appl. Catal., B*, 2022, **306**, 121094.
51 Y. Li, X. Tan, R. K. Hocking, X. Bo, H. Ren, B. Johannessen, S. C. Smith and C. Zhao, *Nat. Commun.*, 2020, **11**, 2720.
52 R. Zhao, Y. Wang, G. Ji, J. Zhong, F. Zhang, M. Chen, S. Tong, P. Wang, Z. Wu, B. Han and Z. Liu, *Adv. Mater.*, 2023, **35**, 2205262.
53 B. Barbee, B. Muchharla, A. Adedeji, A. Karoui, K. Kumar Sadasivuni, M. S. Sha, A. M. Abdullah, G. Slaughter and B. Kumar, *Sci. Rep.*, 2022, **12**, 7507.
54 X. Lv, R. Tan, X. Xu, Y. Li, C. Geng, Y. Fang, C. Tan, B. Cui and L. Wang, *J. Appl. Electrochem.*, 2022, **52**, 895–905.
55 H. Wei, Q. Xue, A. Li, T. Wan, Y. Huang, D. Cui, D. Pan, B. Dong, R. Wei, N. Naik and Z. Guo, *Sens. Actuators, B*, 2021, **337**, 129687.
56 X. Wang, X. Chi, Z. Fu, Y. Xiong, S. Li, Y. Yao, K. Zhang, Y. Li, S. Wang, R. Zhao, Z. Yang and Y.-M. Yan, *Appl. Catal., B*, 2023, **322**, 122130.
57 H.-J. Shin, W. M. Choi, D. Choi, G. H. Han, S.-M. Yoon, H.-K. Park, S.-W. Kim, Y. W. Jin, S. Y. Lee, J. M. Kim, J.-Y. Choi and Y. H. Lee, *J. Am. Chem. Soc.*, 2010, **132**, 15603–15609.
58 M. Kumar and T. C. Nagaiah, *J. Mater. Chem. A*, 2022, **10**, 13031–13041.
59 M. Goswami, S. Kumar, N. Singh, N. Sathish, M. Ashiq and S. Kumar, *Ionics*, 2021, **27**, 5277–5285.
60 P. V. F. de Sousa, A. F. de Oliveira, A. A. da Silva and R. P. Lopes, *Environ. Sci. Pollut. Res.*, 2019, **26**, 14883–14903.
61 M. Lu, N. Gao, X.-J. Zhang and G.-S. Wang, *RSC Adv.*, 2019, **9**, 5550–5556.
62 W. Yu, J. Yu, M. Huang, Y. Wang, Y. Wang, J. Li, H. Liu and W. Zhou, *Energy Environ. Sci.*, 2023, **16**, 2991–3001.
63 R. Zhang, Y. Guo, S. Zhang, D. Chen, Y. Zhao, Z. Huang, L. Ma, P. Li, Q. Yang and G. Liang, *Adv. Energy Mater.*, 2022, **12**, 2103872.
64 Y. Cao, D. Li, C. Ding, S. Ye, X. Zhang, H. Chi, L. Liu, Y. Liu, J. Xiao and C. Li, *ACS Catal.*, 2023, **13**, 11902–11909.
65 D. Gupta, A. Kafle, S. Kaur, T. S Thomas, D. Mandal and T. C. Nagaiah, *ACS Appl. Mater. Interfaces*, 2023, **15**, 4033–4043.
66 J. Choi, B. H. R. Suryanto, D. Wang, H.-L. Du, R. Y. Hodgetts, F. M. Ferrero Vallana, D. R. MacFarlane and A. N. Simonov, *Nat. Commun.*, 2020, **11**, 5546.
67 J.-Y. Fang, Q.-Z. Zheng, Y.-Y. Lou, K.-M. Zhao, S.-N. Hu, G. Li, O. Akdim, X.-Y. Huang and S.-G. Sun, *Nat. Commun.*, 2022, **13**, 7899.
68 Y. Zhang, Y. Zhao, Z. Chen, L. Wang, P. Wu and F. Wang, *Electrochim. Acta*, 2018, **291**, 151–160.
69 W. He, J. Zhang, S. Dieckhöfer, S. Varhade, A. C. Brix, A. Lielpetere, S. Seisel, J. R. C. Junqueira and W. Schuhmann, *Nat. Commun.*, 2022, **13**, 1129.
70 Y. Li, Y. K. Go, H. Ooka, D. He, F. Jin, S. H. Kim and R. Nakamura, *Angew. Chem., Int. Ed.*, 2020, **59**, 9744–9750.
71 M. Kumar, N. Thakur, A. Bordoloi, A. Kumar Yadav, S. N. Jha, D. Bhattacharyya, D. Mandal and T. C. Nagaiah, *J. Mater. Chem. A*, 2022, **10**, 11394–11404.
72 E. P. Randviir, *Electrochim. Acta*, 2018, **286**, 179–186.
73 M. Kumar, A. K. Padhan, D. Mandal and T. C. Nagaiah, *Energy Storage Mater.*, 2022, **45**, 1052–1061.
74 L. C. Green, D. A. Wagner, J. Glogowski, P. L. Skipper, J. S. Wishnok and S. R. Tannenbaum, *Anal. Biochem.*, 1982, **126**, 131–138.
75 H. Lucas and J.-P. Petitet, *J. Phys. Chem. A*, 1999, **103**, 8952–8958.
76 F. Lei, K. Li, M. Yang, J. Yu, M. Xu, Y. Zhang, J. Xie, P. Hao, G. Cui and B. Tang, *Inorg. Chem. Front.*, 2022, **9**, 2734–2740.
77 S.-E. Bae, K. L. Stewart and A. A. Gewirth, *J. Am. Chem. Soc.*, 2007, **129**, 10171–10180.
78 D. P. Butcher and A. A. Gewirth, *Nano Energy*, 2016, **29**, 457–465.
79 J.-X. Liu, D. Richards, N. Singh and B. R. Goldsmith, *ACS Catal.*, 2019, **9**, 7052–7064.
80 F.-Y. Chen, Z.-Y. Wu, S. Gupta, D. J. Rivera, S. V. Lambeets, S. Pecaut, J. Y. T. Kim, P. Zhu, Y. Z. Finfrock, D. M. Meira, G. King, G. Gao, W. Xu, D. A. Cullen, H. Zhou, Y. Han, D. E. Perea, C. L. Muhich and H. Wang, *Nat. Nanotechnol.*, 2022, **17**, 759–767.

